nature synthesis

Article

https://doi.org/10.1038/s44160-023-00307-5

Metal halide perovskite nanorods with tailored dimensions, compositions and stabilities

Received: 29 August 2022

Accepted: 30 March 2023

Published online: 1 May 2023

Check for updates

Shuang Liang[1,2], Mingyue Zhang[1], Sheng He[3], Mengkun Tian[4], Woosung Choi[1], Tianquan Lian[3] & Zhiqun Lin[1,5]

The colloidal synthesis of one-dimensional metal halide perovskite nanocrystals with precisely controlled diameter (D) and length (L) values is challenging due to the intrinsic structural symmetry and ionic crystal nature of the perovskites. This hinders investigation into their size- and shape-dependent properties and prevents their application. Here we report a general platform of cylindrical unimolecular nanoreactors to synthesize a library of one-dimensional perovskite nanorods (NRs) with tailored dimensions ($D \approx 7$–16 nm; $L \approx 40$–220 nm), compositions (all-inorganic perovskites; organic–inorganic perovskites; lead-free double perovskites) and enhanced colloidal, photo, polar-solvent and thermal stabilities. The dependence of the charge-carrier dynamics, photoluminescence quantum yield and optical anisotropy of the perovskite NRs on the diameter and length was examined. Decreasing the diameter yields opposite trends in the photoluminescence quantum yields and charge-carrier dynamics to that of increasing the length. In addition, enhanced structural anisotropy (that is, a higher aspect ratio of L/D) always increases the optical anisotropy of the perovskite NRs. By leveraging the cylindrical unimolecules as nanoreactors, a rich variety of uniform perovskite NRs with controllable dimensions, compositions and enhanced stabilities can be designed for use as building blocks for a variety of applications, such as in optoelectronic devices, catalysis and sensors.

Recently, significant advances have been made in synthesizing nanocrystals (NCs) of metal halide perovskites (ABX_3; A = monovalent organic or inorganic cation; B = divalent inorganic cation; X = halide ion) for applications in solar cells[1], light-emitting diodes[2], photodetectors[3], lasers[4] and scintillators[5]. In contrast to their isotropic nanoparticle counterparts, one-dimensional (1D) perovskite NRs have interesting characteristics due to their structural anisotropy, which include linearly polarized light emission[6], a tunable Auger recombination rate[7] and enhanced charge-carrier transport[8], rendering them an outstanding class of semiconducting nanomaterials for displays[9], lasers[10] and catalysis[11], as well as other applications[12]. However, the ionic crystal nature of metal halide perovskites yields extremely fast growth kinetics and the formation of NCs within seconds[13] during colloidal synthesis, thereby leading to difficulty in regulating the NC morphology

[1]School of Materials Science and Engineering, Georgia Institute of Technology, Atlanta, GA, USA. [2]School of Chemical and Biomolecular Engineering, Georgia Institute of Technology, Atlanta, GA, USA. [3]Department of Chemistry, Emory University, Atlanta, GA, USA. [4]The Institute for Electronics and Nanotechnology, Georgia Institute of Technology, Atlanta, GA, USA. [5]Department of Chemical and Biomolecular Engineering, National University of Singapore, Singapore, Singapore. e-mail: z.lin@nus.edu.sg

https://doi.org/10.1038/s44160-023-00307-5

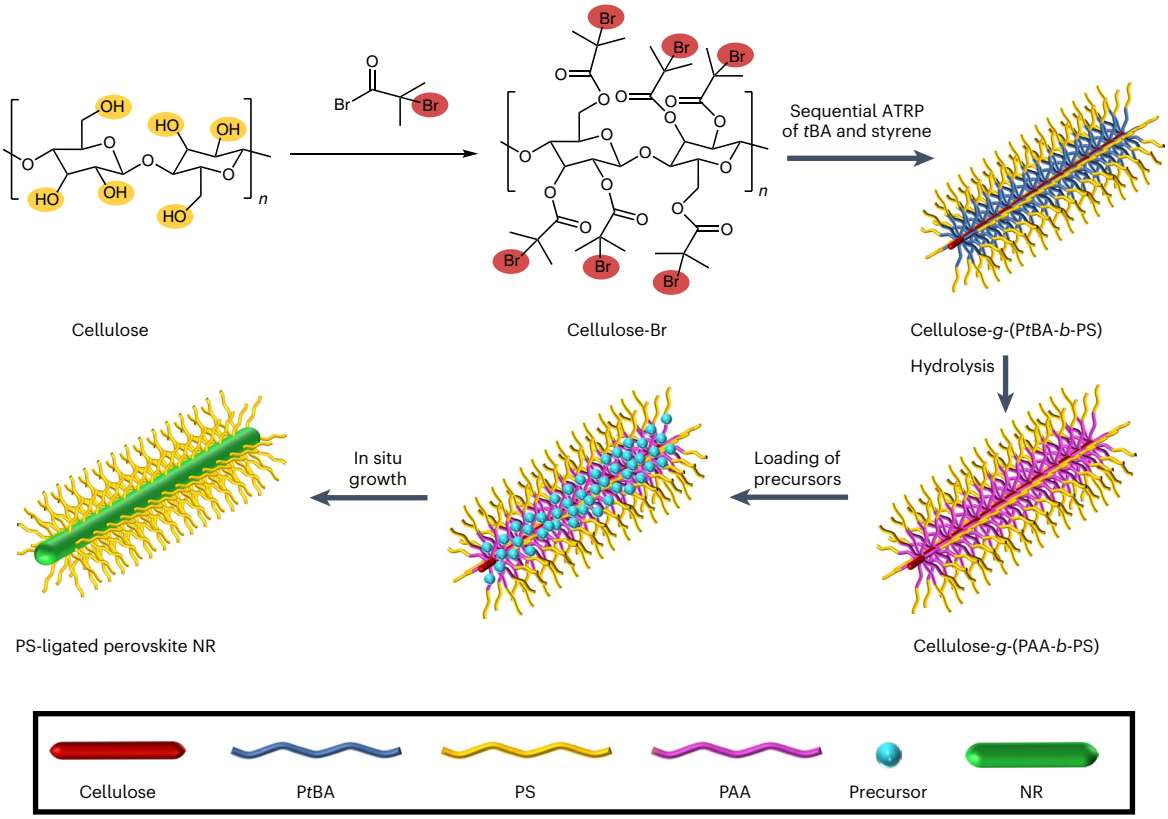

Fig. 1 | Schematic representation of the synthesis of PS-ligated metal halide perovskite NRs. A cylindrical unimolecular cellulose-*g*-(PAA-*b*-PS) BBCP is used as the nanoreactor.

from their thermodynamically stable forms[14]. Moreover, the symmetric crystal structure of both the cubic and orthorhombic phases of perovskites presents an additional challenge for their oriented growth into perovskite NRs[9]. So far, much effort has been centred on producing perovskite NRs via either colloidal synthesis (for example, hot-injection[15], ligand-assisted reprecipitation[7] and tip ultrasonication[16]) or post-synthesis modification (such as seed-mediated growth[9–11], interfacial synthesis[17] and chemical cutting[18]). Nonetheless, these methods are limited in scope since either only a certain type of perovskite NR can be synthesized or the dimensions of the NRs, the diameter in particular, cannot be tuned. Clearly, a synthesis protocol that enables the creation of a diversity of perovskite NRs of interest that concurrently possess monodisperse yet tailorable diameter and length values has yet to be explored.

The colloidal synthesis of perovskite NCs often involves the use of small organic molecules as ligands to stabilize the NCs and passivate surface defects[14]. Nevertheless, the dynamic binding characteristics of these ligands to the perovskite NCs unavoidably leads to ligand dissociation during the purification and storage of perovskite NCs[19], resulting in incomplete surface coverage and the tendency for aggregation. Thus, taking this issue together with their intrinsic ionic crystal nature, perovskite NCs display limited colloidal stability and easily decompose on exposure to moisture, heat, ultraviolet light and polar solvents[12,20]. Strikingly, even in non-polar solvents (such as cyclohexane), long perovskite nanowires have been found to transform morphologically into shorter NRs during storage due to ligand dissociation and crystal dissolution[18], thus unfavourably altering their optical properties. Forming perovskite NRs via post-synthesis modification generally involves exposure of the perovskite NCs to polar solvents[16,17], which potentially decreases the stability of the resulting perovskite NRs and triggers detrimental defects in their crystal lattices. The reliable synthesis of various perovskite NRs with uniform morphologies, tailorable dimensions and compositions as well as superior structural stability and thus integrity of their properties represents a crucial step that underpins future advances in perovskite NR-based materials and devices, which is of both fundamental and practical importance. However, effective strategies to yield perovskite NRs that simultaneously meet all of the above-described characteristics remain elusive.

Here we report a universal and robust platform for the precision synthesis of a large range of uniform 1D perovskite NRs with meticulously varied diameters and lengths to unravel not only their strong dimension-dependent charge-carrier dynamics, photoluminescence quantum yield (PLQY) and optical anisotropy but also their outstanding stabilities. The signature of our platform lies in directing the growth of polymer-ligated perovskite NRs of interest by capitalizing on a set of amphiphilic bottlebrush block copolymers (BBCPs) as nanoreactors. Specifically, a series of amphiphilic cellulose-*graft*-[poly(acrylic acid)-*block*-polystyrene] (cellulose-*g*-(PAA-*b*-PS)) BBCPs with a well-defined molecular weight (MW) of the inner PAA and outer PS blocks and a narrow MW distribution are synthesized via atom transfer radical polymerization (ATRP) from a cellulose backbone. They form cylindrical unimolecular micelles in solution, thus functioning as nanoreactors for crafting PS-ligated perovskite NRs via strong coordination interactions between the inner PAA blocks and the precursors. Notably, the diameter (D) and length (L) of the perovskite NRs are dictated by the MWs of the inner hydrophilic PAA blocks and the cellulose backbone, which can be readily regulated by controlling the ATRP time of the *tert*-butyl acrylate (*t*BA) monomers and the fractional precipitation of brominated cellulose (cellulose-Br), respectively. As a result, the aspect ratio (AR) values of the perovskite NRs (such as caesium lead bromide ($CsPbBr_3$), an all-inorganic perovskite) can be tuned easily in either the radial (at a fixed L) or axial (at a given D) direction. Moreover, simply altering the choice of precursors renders the synthesis of a wide range of perovskite NRs with various compositions

https://doi.org/10.1038/s44160-023-00307-5

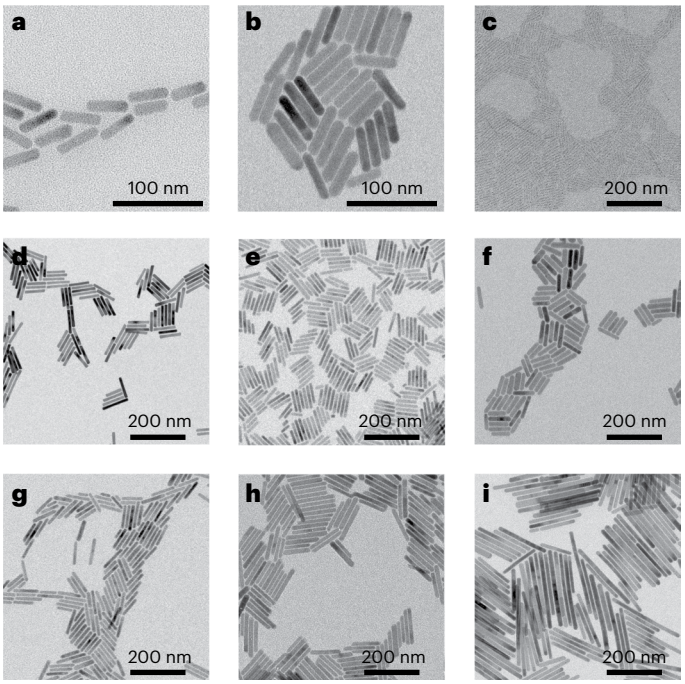

Fig. 2 | TEM images of PS-ligated $CsPbBr_3$ NRs with various *D* and *L* values. **a**, $D = 10.1 \pm 0.8$ nm and $L = 41.4 \pm 3.7$ nm. **b**, $D = 10.0 \pm 1.8$ nm and $L = 52.2 \pm 8.9$ nm. **c**, $D = 6.6 \pm 0.5$ nm and $L = 76.3 \pm 21.6$ nm. **d**, $D = 9.7 \pm 1.0$ nm and $L = 80.0 \pm 13.3$ nm. **e**, $D = 12.3 \pm 1.7$ nm and $L = 81.8 \pm 16.4$ nm. **f**, $D = 16.2 \pm 1.2$ nm and $L = 79.4 \pm 11.7$ nm. **g**, $D = 10.0 \pm 0.9$ nm and $L = 90.7 \pm 11.4$ nm. **h**, $D = 10.2 \pm 1.7$ nm and $L = 115.6 \pm 20.3$ nm. **i**, $D = 10.4 \pm 1.1$ nm and $L = 217.2 \pm 31.4$ nm.

of the A, B and X sites, including methylammonium lead bromide ($MAPbBr_3$; an organic–inorganic perovskite), formamidinium lead bromide ($FAPbBr_3$; another organic–inorganic perovskite), caesium silver bismuth bromide ($Cs_2AgBiBr_6$; a lead-free double perovskite), caesium lead chloride ($CsPbCl_3$; an all-inorganic perovskite with varied X sites), caesium lead bromide/chloride ($CsPb(Br/Cl)_3$; an all-inorganic perovskite with hybrid X sites), caesium lead iodide/bromide ($CsPb(I/Br)_3$; another all-inorganic perovskite with hybrid X sites) and caesium lead iodide ($CsPbI_3$; another all-inorganic perovskite), corroborating the generality and viability of our platform of cylindrical unimolecular nanoreactors.

For the perovskite NRs, decreasing *D* at a constant *L* and increasing *L* at a fixed *D* yields opposite trends in their PLQY values and charge-carrier dynamics, which is reflected by their average photoluminescence (PL) lifetimes. Specifically, decreasing the diameter of a perovskite NR below its Bohr diameter (D_{Bohr}) strengthens quantum confinement, leading to an increased PLQY with a shortened average PL lifetime. Conversely, elongating the *L* of a perovskite NR that far exceeds its D_{Bohr} results in a reduced PLQY and a prolonged average PL lifetime due to the possibility of the NR-length-dependent trapping-and-detrapping process of excitons. It is also interesting to note that the enhanced structural anisotropy (that is, the higher AR) fosters an increase in optical anisotropy, regardless of tailoring of the dimension in the radial or axial direction. Finally, in sharp contrast to possible ligand-dissociation issues, as noted in past studies on perovskite NCs, the intimate and strong tethering of hydrophobic PS chains on the surface of the perovskite NR affords a stable polymer shell that acts as a physical barrier to retard the diffusion of moisture and polar solvents on a single-NR level, thereby markedly enhancing the colloidal, photo, polar-solvent and thermal stabilities of perovskite NRs. With designer dimensions, compositions and stabilities, such perovskite NRs expand the scope of perovskite NCs through the introduction of anisotropic structures and properties (such as a continuous pathway along the axial direction for transporting carriers), and will provide opportunities for their exploitation as building blocks to create a variety of assemblies and materials with additional functionalities, for use in applications such as optoelectronics, catalysis and sensors.

Results and discussion

Synthesis of PS-ligated perovskite NRs

Figure 1 depicts the general synthetic route to the PS-ligated metal halide perovskite NRs. Specifically, cellulose, a natural polymer with a rigid backbone[21], was first dissolved in the 1-allyl-3-methylimidazolium chloride ionic liquid to break all inter- and intra-molecular hydrogen bonds between the hydroxyl groups along the cellulose backbone. Afterwards, the hydroxyl groups of cellulose were converted into ω-bromo terminal groups (forming cellulose-Br) via esterification with α-bromoisobutyryl bromide (BiBB). To increase the conversion of hydroxyl groups to terminal bromo groups, a second esterification step in *N*-methylpyrrolidone with BiBB was conducted, leading to nearly 100% conversion as confirmed via ^{1}H NMR spectroscopy (Supplementary Fig. 1). After esterification, the cellulose-Br can be readily dissolved in many organic solvents (such as acetone and tetrahydrofuran) and used as a macroinitiator for sequential ATRP to prepare a series of BBCPs (see the Experimental section in the Supplementary Information). The chain length of the cellulose-Br dictates the length of the resulting BBCPs and later template-grown inorganic NRs. However, natural cellulose typically has a wide MW distribution, which thus results in a large size distribution of the as-prepared BBCPs and NRs. Supplementary Figure 2 shows that the raw cellulose-Br possesses a high polydispersity index (PDI) of 3.3. Thus, fractional precipitation of the cellulose-Br was carried out to achieve a narrow MW distribution (PDI < 1.3) (Supplementary Fig. 3 and Supplementary Table 1). Subsequently, cellulose-Br with a low PDI was used as the macroinitiator for the sequential ATRP of *t*BA and styrene, followed by hydrolysis of the inner poly(*tert*-butyl acrylate) (P*t*BA) blocks to form cellulose-*g*-(PAA-*b*-PS) BBCPs (Fig. 1, lower right). ^{1}H NMR analysis of cellulose-*g*-P*t*BA, cellulose-*g*-(P*t*BA-*b*-PS) and cellulose-*g*-(PAA-*b*-PS) is shown in Supplementary Figs. 4–6, respectively. As shown in Supplementary Table 2, nine cellulose-*g*-(PAA-*b*-PS) BBCPs were synthesized using different MWs of either the cellulose-Br macroinitiator or the PAA blocks, via controlling the ATRP time of the *t*BA monomers. Typical atomic force microscopy images are shown in Supplementary Fig. 7 to substantiate the success of synthesizing the cellulose-*g*-(PAA-*b*-PS) BBCPs with a 1D cylindrical structure and, more importantly, tailorable dimensions. For instance, the cellulose-*g*-(PAA-*b*-PS)-2 BBCPs (Supplementary Fig. 7a) possessed *L* and *D* values of approximately 60 nm and 25 nm, respectively, as determined from the height profile in Supplementary Fig. 7e. By contrast, using similar MW (length) values of the PAA and PS blocks per arm yet a different MW for cellulose-Br (Supplementary Table 2), the cellulose-*g*-(PAA-*b*-PS)-8 BBCPs displayed a similar *D* value of 25 nm but a different *L* value of 120 nm (Supplementary Fig. 7c,e).

The cellulose-*g*-(PAA-*b*-PS) BBCPs are composed of densely grafted PAA-*b*-PS side chains with well-defined MWs and a narrow MW distribution of the PAA and PS blocks along the cellulose backbone (with three PAA-*b*-PS chains per repeat unit of cellulose)[22]. These BBCPs were then used as nanoreactors to prepare uniform, PS-ligated perovskite NRs with intimately and firmly tethered hydrophobic PS blocks. Cellulose-*g*-(PAA-*b*-PS) BBCPs were first dissolved in anhydrous dimethylformamide (DMF) to form stable, cylindrical unimolecular micelles with fully expanded PAA and PS chains due to the good solvent characteristics of DMF. On addition of the perovskite precursors (for example, CsBr and $PbBr_2$ for $CsPbBr_3$), owing to the strong coordination interactions between the metal moieties of the precursors and the carboxylic acid groups of the PAA chains[23], the perovskite precursors (represented as light blue spheres in Fig. 1) were selectively loaded into the cylindrical

https://doi.org/10.1038/s44160-023-00307-5

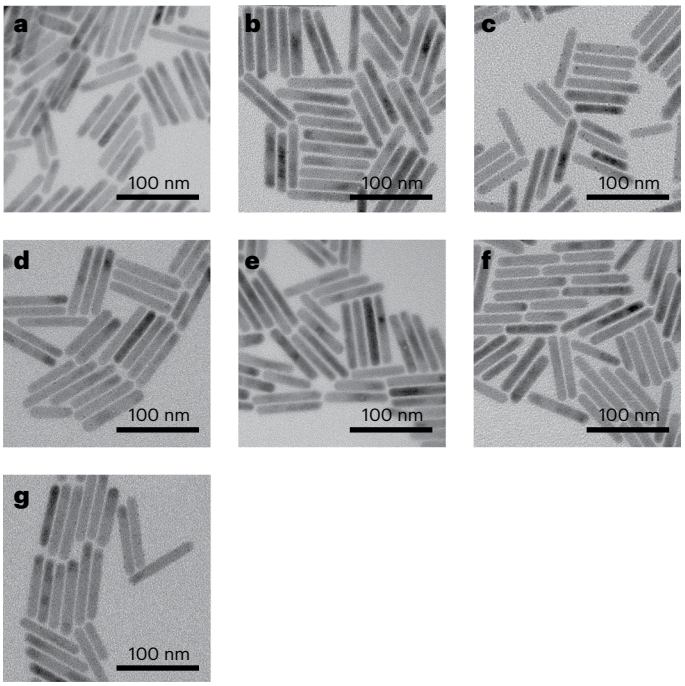

Fig. 3 | TEM images of PS-ligated perovskite NRs of different compositions. **a**, $MAPbBr_3$ NRs (organic–inorganic perovskite; $D = 9.8 \pm 0.7$ nm and $L = 75.4 \pm 18.8$ nm). **b**, $FAPbBr_3$ NRs (organic–inorganic perovskite; $D = 10.7 \pm 1.6$ nm and $L = 77.9 \pm 8.8$ nm). **c**, $Cs_2AgBiBr_6$ NRs (lead-free double perovskite; $D = 9.3 \pm 0.8$ nm and $L = 77.9 \pm 20.1$ nm). **d**, $CsPbCl_3$ NRs (all-inorganic perovskite with varied X sites; $D = 10.1 \pm 1.2$ nm and $L = 81.4 \pm 13.3$ nm). **e**, $CsPb(Br/Cl)_3$ NRs (all-inorganic perovskite with hybrid X sites; $D = 10.2 \pm 1.0$ nm and $L = 76.1 \pm 10.0$ nm). **f**, $CsPb(I/Br)_3$ NRs (all-inorganic perovskite with hybrid X sites; $D = 10.4 \pm 0.8$ nm and $L = 77.9 \pm 13.0$ nm). **g**, $CsPbI_3$ NRs (all-inorganic perovskite with varied X site; $D = 9.4 \pm 1.1$ nm and $L = 82.9 \pm 15.3$ nm). All as-prepared perovskite NRs exhibit similar dimensions, achieved using cellulose-*g*-(PAA-*b*-PS)-4 as the nanoreactor (Supplementary Table 2).

compartment occupied by the expanded PAA chains. Afterwards, the solution containing the precursor-loaded cellulose-*g*-(PAA-*b*-PS) BBCPs was injected quickly into toluene at 50 °C. Because of the poor solubility of the perovskite precursors in toluene, the perovskite NR was formed rapidly in the PAA compartment with PS chains ligated on its surface (lower left panel, Fig. 1, lower left) thus yielding the PS-ligated NR. Owing to the original covalent bonding of the PS and PAA blocks, the PS chains are permanently situated on the surface of the perovskite NR without any occurrence of the ligand-dissociation issue that is commonly encountered in perovskite NCs synthesized via conventional approaches[24]. As a result, PS-ligated perovskite NRs can be well dispersed in toluene without precipitation after three rounds of alternative washing using toluene as a good solvent and ethyl acetate as a poor solvent.

Figure 2 presents the representative transmittance electron microscopy (TEM) images of an array of PS-ligated $CsPbBr_3$ NRs with various *D* and *L* values, template-grown by capitalizing on nine different BBCPs (that is, cellulose-*g*-(PAA-*b*-PS)-1 to cellulose-*g*-(PAA-*b*-PS)-9 in Supplementary Table 2). As shown in Supplementary Fig. 8, the X-ray diffraction patterns of the as-prepared $CsPbBr_3$ NRs match well with the characteristic peaks of the orthorhombic phase or cubic phase of $CsPbBr_3$ (ref. 25), indicating the successful synthesis of $CsPbBr_3$ NRs. The orthorhombic phase of $CsPbBr_3$ exhibits two peaks around 30°, whereas the cubic phase manifests a single peak at 30°. However, it is difficult to conclusively determine the exact phase due to the peak broadening that originates from the small size of these NRs, despite the asymmetric peaks around 30° potentially suggesting the existence of the orthorhombic phase[8,25]. To demonstrate the ability of our unique platform of cylindrical unimolecular nanoreactors to regulate the dimensions of the NRs both radially and axially, two sets of PS-ligated $CsPbBr_3$ NRs were crafted. The first set involves the NRs of various *L* values at a fixed *D*. Specifically, cellulose-Br with different MWs was used as the macroinitiator to synthesize P*t*BA of nearly the same MW per arm, which was then converted into PAA via hydrolysis (Supplementary Table 2). Therefore, using cellulose-Br with a progressively increasing MW from 8,000 g mol^{-1} to 41,500 g mol^{-1} at a similar MW of PAA per arm yielded perovskite NRs with a similar *D* yet an increasing *L*. As shown in Fig. 2a,b,d,g–i, PS-ligated $CsPbBr_3$ NRs have a fixed *D* of around 10 nm but different *L* values (41.4 ± 3.7 nm in Fig. 2a, templated from cellulose-*g*-(PAA-*b*-PS)-1; 52.2 ± 8.9 nm in Fig. 2b from cellulose-*g*-(PAA-*b*-PS)-2; 80.0 ± 13.3 nm in Fig. 2d from cellulose-*g*-(PAA-*b*-PS)-4; 90.7 ± 11.4 nm in Fig. 2g from cellulose-*g*-(PAA-*b*-PS)-7, 115.6 ± 20.3 nm in Fig. 2h from cellulose-*g*-(PAA-*b*-PS)-8; 217.2 ± 31.4 nm in Fig. 2i from cellulose-*g*-(PAA-*b*-PS)-9). It is worth noting that the length distribution of these $CsPbBr_3$ NRs is generally ~15%, which correlated well with the PDI of the cellulose-Br macroinitiator used to prepare the cellulose-*g*-(PAA-*b*-PS) BBCPs. As a result, the AR of the as-crafted $CsPbBr_3$ NRs can be readily tuned from ~4 (AR = *L*/*D* = 41.4/10.1) to ~21 (AR = *L*/*D* = 217.2/10.4) for a given *D*.

The second set of PS-ligated $CsPbBr_3$ NRs synthesized using the cylindrical unimolecular cellulose-*g*-(PAA-*b*-PS) nanoreactors entails NRs of various *D* values at a fixed *L*. Owing to the living polymerization characteristic of ATRP[22], the MW of the PAA blocks can be easily tailored by adjusting the ATRP time of the P*t*BA blocks followed by hydrolysis to PAA. Four cellulose-*g*-(PAA-*b*-PS) BBCPs were synthesized using the same cellulose-Br as the macroinitiator (MW = 13,100 g mol^{-1}) but grafting different lengths of PAA blocks per arm (6,100 g mol^{-1}, cellulose-*g*-(PAA-*b*-PS)-3; 9,200 g mol^{-1}, cellulose-*g*-(PAA-*b*-PS)-4; 11,900 g mol^{-1}, cellulose-*g*-(PAA-*b*-PS)-5; 12,800 g mol^{-1}, cellulose-*g*-(PAA-*b*-PS)-6; Supplementary Table 2). Consequently, the resulting $CsPbBr_3$ NRs demonstrate a comparable *L* of ~80 nm yet various *D* values, of 6.6 ± 0.5 nm (Fig. 2c), 9.7 ± 1.0 nm (Fig. 2d), 12.3 ± 1.7 nm (Fig. 2e) and 16.2 ± 1.2 nm (Fig. 2f). Thus, the AR values of these PS-ligated $CsPbBr_3$ NRs are approximately 12, 8, 7 and 5, respectively. Taken together, our nanoreactor platform renders the creation of uniform 1D perovskite NRs with tailorable *D* and *L* values, which has not yet been achieved using other approaches. A series of control experiments was conducted to justify the importance of exploiting cellulose-*g*-(PAA-*b*-PS) BBCPs as nanoreactors to direct the growth of NRs and control their dimensions (Supplementary Figs. 12–14).

To validate the versatility of the nanoreactor platform further, seven different types of perovskite NR ($MAPbBr_3$, $FAPbBr_3$, $Cs_2AgBiBr_6$, $CsPbCl_3$, $CsPb(Br/Cl)_3$, $CsPb(I/Br)_3$ and $CsPbI_3$) were also synthesized under the same reaction conditions. Their TEM images (Fig. 3) and X-ray diffraction spectra (Supplementary Fig. 17) corroborate the successful production of these NRs. Compared with all-inorganic perovskites, organic–inorganic hybrid perovskites with organic A-site cations display additional structural flexibility and a better performance in optoelectronics[26]. However, owing to the readily volatile nature and dynamic motion of the organic A sites[14], this class of perovskite NCs exhibits a relatively low stability at elevated temperatures as well as limited structural integrity over their all-inorganic counterpart[19], which poses significant challenges in producing uniform 1D organic–inorganic hybrid perovskite NRs. Therefore, it is particularly notable that our platform of cylindrical BBCP nanoreactors is robust and can enable the synthesis of organic–inorganic hybrid perovskite NRs that would otherwise be difficult to achieve. As examples, 1D $MAPbBr_3$ and $FAPbBr_3$ were yielded by simply replacing CsBr with MABr and FABr as the precursor, respectively, and using the cellulose-*g*-(PAA-*b*-PS)-4 BBCP as the nanoreactor (see Methods and the Experimental section in the Supplementary Information). The PS-ligated $MAPbBr_3$ NRs (Fig. 3a) have an average $D = 9.8 \pm 0.7$ nm and $L = 75.4 \pm 18.8$ nm, and

the PS-ligated $FAPbBr_3$ NRs (Fig. 3b) have an average $D = 10.7 \pm 1.6$ nm and $L = 77.9 \pm 8.8$ nm, which are similar to the PS-ligated $CsPbBr_3$ NRs discussed above ($D = 9.7 \pm 1.0$ nm and $L = 80.0 \pm 13.3$ nm) synthesized using the same nanoreactor.

Nanorods of 1D $Cs_2AgBiBr_6$, a lead-free double perovskite, were also synthesized (Fig. 3c). Lead-free perovskites represent an important class of metal halide perovskite materials as they dispense with the toxic element lead, which is of great fundamental and practical significance[27]. In this context, the perovskite precursor $PbBr_2$ was substituted with $BiBr_3$ and AgBr to produce the lead-free $Cs_2AgBiBr_6$ NRs. Likewise, using the cellulose-*g*-(PAA-*b*-PS)-4 BBCP as the nanoreactor yielded PS-ligated $Cs_2AgBiBr_6$ NRs with $D = 9.3 \pm 0.8$ nm and $L = 77.9 \pm 20.1$ nm, indicating the capability of our nanoreactor platform for crafting perovskite NRs with desirable metal compositions. Furthermore, this platform can be conveniently applied to grow metal halide perovskites of different halides (varied and hybrid X sites; Fig. 3d–g). Replacing the bromide-containing precursors with chloride- and iodide-containing precursors or their combinations, and again using the cellulose-*g*-(PAA-*b*-PS)-4 BBCP as the nanoreactor, the synthesis of PS-ligated $CsPbCl_3$, $CsPb(Br/Cl)_3$, $CsPb(I/Br)_3$ and $CsPbI_3$ NRs, respectively, was achieved. These NRs show similar dimensions to the other three types of perovskite NR discussed above (that is, $D = 10.1 \pm 1.2$ nm and $L = 81.4 \pm 13.3$ nm for $CsPbCl_3$ NRs, $D = 10.2 \pm 1.0$ nm and $L = 76.1 \pm 10.0$ nm for $CsPb(Br/Cl)_3$ NRs, $D = 10.4 \pm 0.8$ nm and $L = 77.9 \pm 13.0$ nm for $CsPb(I/Br)_3$ NRs, $D = 9.4 \pm 1.1$ nm and $L = 82.9 \pm 15.3$ nm for $CsPbI_3$ NRs). Our one-step, direct synthesis of $CsPbCl_3$ and $CsPbI_3$ NRs circumvents the potential issue of defect generation (such as halide vacancies), incomplete halide substitution and the formation of heterogeneous domains with ambiguous halide compositions, which are commonly seen in $CsPbCl_3$ and $CsPbI_3$ NCs prepared via post-synthesis processes[14,25]. We note that the black dots seen in some of the TEM images of the perovskite NRs are generated through electron-beam-induced degradation (for example, Fig. 3c), which has been well documented because of the limited stability of perovskites under high-energy electron beams.

Intriguingly, as observed clearly in Fig. 4a, the $CsPbBr_3$ NR shows $D \approx 12$ nm and a thin shell with a lower contrast of ~6 nm thickness (t_{shell}) that conformally covers the entire surface of the NR, indicating the presence of a protective polymeric shell (PS chains). The MW of the PAA block per arm is comparable to that of the PS block per arm in the cellulose-*g*-(PAA-*b*-PS)-8 BBCP nanoreactor; thus, the resulting $CsPbBr_3$ NRs display a D value of around twice the thickness of the PS shell visualized (that is, $2t_{shell}$). Moreover, as shown in Supplementary Fig. 7c,e, the atomic force microscopy image and the corresponding height profile of the cellulose-*g*-(PAA-*b*-PS)-8 BBCP suggest a height of roughly 25 nm, similar to the sum of the $CsPbBr_3$ NR D value and $2t_{shell}$ of the PS shell observed via TEM, suggesting that the formation of 1D perovskite NRs is indeed directed by the cellulose-*g*-(PAA-*b*-PS) BBCP nanoreactor.

High-angle annular dark-field scanning TEM (HAADF-STEM) images with atomic resolution for PS-ligated $CsPbCl_3$ NRs, $CsPbBr_3$ NRs and $CsPbI_3$ NRs are shown in Fig. 4b–d, respectively. Generally, the synthesis of 1D NCs requires facet selection and the control of anisotropic growth in the selected facet of the NC[28]. However, the interplanar distances of the planes perpendicular to the axial direction of the NRs are 0.56 nm, 0.58 nm and 0.32 nm for the $CsPbCl_3$ NRs, $CsPbBr_3$ NRs and $CsPbI_3$ NRs, respectively, which correspond to the (100) facet of cubic phase $CsPbCl_3$ (ref. 29), the (110) or (002) facet of orthorhombic phase $CsPbBr_3$ (ref. 30) and the (200) facet of cubic phase $CsPbI_3$ (ref. 31). On the basis of these results, the perovskite NRs synthesized by our unique nanoreactor platform probably did not grow along any particular facet or direction, which has also been reported in perovskite NRs synthesized via other methods[8,32]. The NRs were potentially yielded from the confined nucleation and growth of perovskite NCs within the anisotropic, 1D compartment occupied by the PAA blocks. The PS-ligated $CsPbBr_3$ NR shown in Supplementary Fig. 18 exhibits three distinctive crystalline domains along the axial direction, signifying that the NR may have been created by multiple nucleation sites that eventually grew into a single NR inside the BBCP nanoreactor, due to the intrinsic 1D architecture of the BBCP. However, it is important to note that the oriented growth of 1D perovskite NRs followed by twisting may also yield a similar observation[30]; this merits further investigation on whether or not PAA chains will selectively bind to a specific facet of the perovskite to impart the growth of NRs along a certain direction before twisting occurs to produce polycrystalline perovskite NRs.

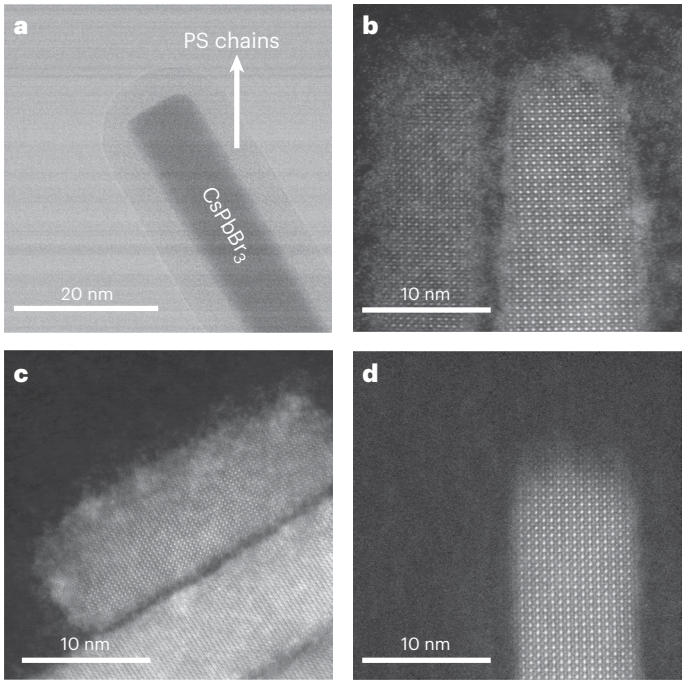

Fig. 4 | TEM and HAADF-STEM images of PS-ligated caesium lead halide perovskite NRs. a, TEM image of a PS-ligated $CsPbBr_3$ NR synthesized from the cellulose-*g*-(PAA-*b*-PS)-8 BBCP, showing a shell layer of PS uniformly tethered on the NR surface. **b**–**d**, HAADF-STEM images with atomic resolution for $CsPbCl_3$ NRs (**b**), $CsPbBr_3$ NRs (**c**) and $CsPbI_3$ NRs (**d**) synthesized from the cellulose-*g*-(PAA-*b*-PS)-4 BBCP.

Dimension-dependent photophysical properties

Clearly, our general BBCP nanoreactor platform imparts the creation of a rich variety of 1D perovskite NRs with tailored dimensions and compositions. As such, they afford a unique opportunity for scrutinizing the dimension-dependent photophysical properties of perovskite NRs by decoupling the respective effect between D and L, that is, systematically varying D while fixing L and vice versa. Specifically, we carried out steady-state UV-visible absorption spectroscopy and PL spectroscopy on two series of PS-ligated $CsPbBr_3$ NRs: altering D from ~16 nm to ~7 nm at a fixed L of ~80 nm (Supplementary Fig. 19); and adjusting L from ~40 nm to ~220 nm at a constant D of ~10 nm (Supplementary Fig. 20).

First, the effect of the NR diameter on their optical properties was elucidated. $CsPbBr_3$ possesses an effective D_{Bohr} of 7 nm (refs. 33,34), suggesting a quantum confinement effect on its optical properties when D is close to or below 7 nm and a weakly confined regime from 7 nm to 18 nm. At a fixed L of ~80 nm, when decreasing the D value of the $CsPbBr_3$ NRs from 16.2 nm to 12.3 nm, 9.7 nm and 6.6 nm (that is, increasing the AR from ~5 to ~7, ~8, and ~12) (Supplementary Table 2), both the PL (from 515 nm to 514 nm, 512 nm and 502 nm) and UV-visible peak positions (from 512 nm to 508 nm, 506 nm and 484 nm)

https://doi.org/10.1038/s44160-023-00307-5

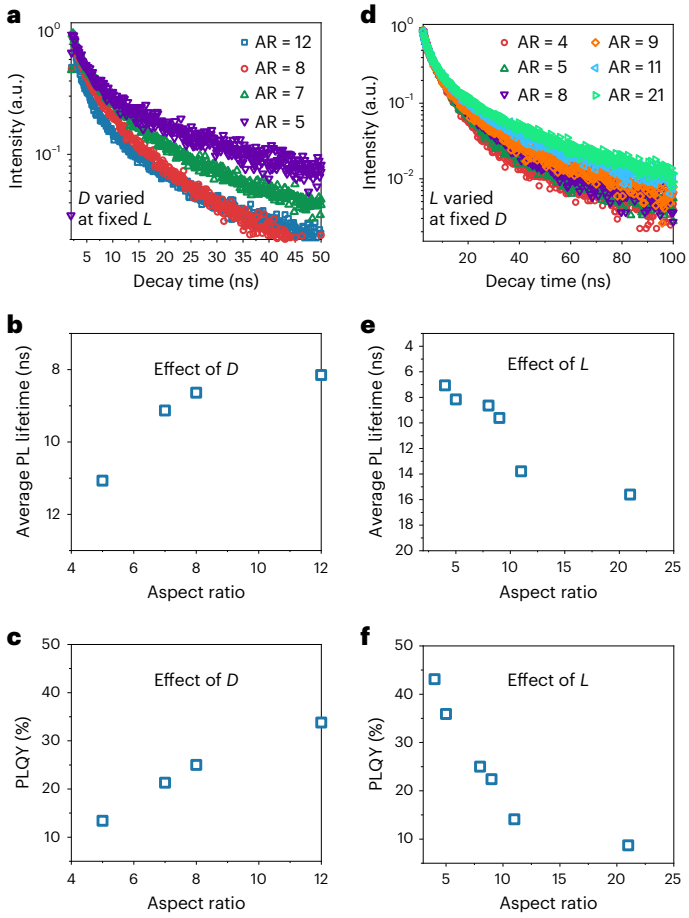

Fig. 5 | Dimension-dependent average PL decay lifetime and PLQY of two sets of PS-ligated $CsPbBr_3$ NRs. a–c, Normalized PL decay kinetics (**a**), average PL decay lifetime (**b**) and absolute PLQY (**c**) as a function of the AR of PS-ligated $CsPbBr_3$ NRs with variation of the NR diameter (D = 16.2 nm (AR ≈ 5), 12.3 nm (AR ≈ 7), 9.7 nm (AR ≈ 8) and 6.6 nm (AR ≈ 12)) at a fixed length (L ≈ 80 nm). **d–f**, Normalized PL decay kinetics (**d**), average PL decay lifetime (**e**) and absolute PLQY (**f**) as a function of the AR with tailoring of the NR length (L = 41.4 nm (AR ≈ 4), 52.2 nm (AR ≈ 5), 80.0 nm (AR ≈ 8), 90.7 nm (AR ≈ 9), 115.6 nm (AR ≈ 11) and 217.2 nm (AR ≈ 21)) at a fixed diameter (D ≈ 10 nm).

were progressively blueshifted, respectively (Supplementary Fig. 19). Reducing the D value of the $CsPbBr_3$ NRs in the weakly confined regime (that is, from 16.2 nm to 9.7 nm) results in a modest increase in the electronic bandgap energy (~14 meV; calculated from the UV-visible spectra). By contrast, further reducing D from 9.7 nm to 6.6 nm in the strongly confined regime (<D_{Bohr}) results in a considerable increase in the electronic bandgap energy (~48 meV) because of the quantum confinement effect[33].

Subsequently, the influence of the NR length on the optical properties was then explored with D fixed at ~10 nm whilst L is varied from 41.4 nm (AR ≈ 4) to 52.2 nm (AR ≈ 5), 80.0 nm (AR ≈ 8), 90.7 nm (AR ≈ 9), 115.6 nm (AR ≈ 11) and 217.2 nm (AR ≈ 21) (Supplementary Fig. 20). A clear redshift of the PL (from 506 nm to 507 nm, 513 nm, 515 nm, 518 nm and 520 nm) and UV-visible peaks (from 499 nm to 502 nm, 507 nm, 511 nm, 515 nm and 516 nm) is seen with the AR increasing from ~4 to ~21. However, as the L values of these NRs exceed the D_{Bohr} of $CsPbBr_3$, drastically increasing the NR length from 41.4 nm to 217.2 nm produces a reduction of only ~66 meV (calculated from the PL spectra) in the electronic bandgap energy, which is comparable to the effect of reducing D from 9.7 nm to 6.6 nm at a fixed L as discussed above (48 meV). Clearly, varying the diameter of the $CsPbBr_3$ NRs exerts a more pronounced effect on the optical properties than varying the length, due to the similar length scale of D to its D_{Bohr}.

Furthermore, the dimension-dependent photogenerated exciton dynamics and the PLQY of the $CsPbBr_3$ NRs were assessed through time-resolved photoluminescence (TRPL) and absolute PLQY measurements, respectively (Fig. 5). The TRPL data were fitted using a bi-exponential decay function with a fast decay time component τ_1 (intrinsic band-to-band recombination of photogenerated charge carriers) and a slow decay time component τ_2 (trap-assisted recombination)—see the section 'Fitting of time-resolved photoluminescence (TRPL) kinetics of NRs' in the Supplementary Information for more details[20]. As shown in Fig. 5a,b and Supplementary Table 3, increasing the AR via decreasing the NR diameter (see the D values above; at a fixed L ≈ 80 nm) clearly facilitated the PL decay and reduced the average PL lifetime (τ_{ave}), from τ_{ave} = 11.07 ns (AR ≈ 5) to τ_{ave} = 9.13 ns (AR ≈ 7), τ_{ave} = 8.64 ns (AR ≈ 8) and τ_{ave} = 8.15 ns (AR ≈ 12). Similar to the findings from zero-dimensional nanoparticles[35] and two-dimensional nanoplatelets[36], the augmented quantum confinement effect of the $CsPbBr_3$ NRs with a reduced diameter contributed to the boosted PLQYs (Fig. 5c), increasing from 13.4% for AR ≈ 5 to 21.3% (AR ≈ 7), 25% (AR ≈ 8) and 33.8% (AR ≈ 12), and accelerated PL decay as summarized in Supplementary Table 3. Notably, the decrease in diameter of the $CsPbBr_3$ NRs near or below their D_{Bohr} value increases the quantum confinement of photogenerated charge carriers. This in turn leads to an enhancement of the exciton binding energy and electron–hole wavefunction overlap and promotes excitonic radiative recombination[35,37], thereby resulting in a shortened τ_{ave} and an increased PLQY.

By contrast, raising the AR via increasing the length of the $CsPbBr_3$ NR (see the L values above; at constant D ≈ 10 nm) shows an opposite trend, as depicted in Fig. 5d–f. Increasing the AR from ~4 to ~5, ~8, ~9, ~12 and ~22 retarded the PL decay and prolonged the τ_{ave}, from τ_{ave} = 7.07 ns (AR ≈ 4) to τ_{ave} = 8.16 ns (AR ≈ 5), τ_{ave} = 8.64 ns (AR ≈ 8), τ_{ave} = 9.61 ns (AR ≈ 9), τ_{ave} = 13.79 ns (AR ≈ 11) and τ_{ave} = 15.61 ns (AR ≈ 21), as well as reducing the PLQY (from 43.1% to 35.9%, 25.0%, 22.4%, 14.1% and 8.7%), respectively (Supplementary Table 4). As noted above, the length of the PS-ligated $CsPbBr_3$ NRs is much larger than D_{Bohr} for $CsPbBr_3$. Thus, regulating the length of the $CsPbBr_3$ NRs will probably not affect the quantum confinement of the photogenerated charge carriers, as shown by their similar τ_1 values (~1.46–3.21 ns). The trap-assisted recombination lifetime τ_2 increases with the NR length (Supplementary Table 4), which can be attributed to either an exciton trapping-and-detrapping process[15,38] or additional transitions from symmetry-forbidden states[34]. Specifically, $CsPbBr_3$ NRs with L < 500–800 nm possess a length-dependent PL decay because of the trapping and detrapping of excitons, due to the high defect tolerance of perovskites[15]. Given the low excitation density in our TRPL experiments and the constant defect density (the number of defects per nanometre) of NRs with different lengths[15], longer NRs will contain the same number of excitons but more defects than shorter NRs, thus lowering the PLQY (Fig. 5f). Such a decrease in the PLQY is consistent with the fitted τ_2 increase in longer NRs (Supplementary Table 4), where more defects in longer NRs render a higher trapping probability and thus a longer trap-assisted recombination lifetime. This is because the detrapped excitons, which occur due to the presence of shallow trap states in perovskites (as noted above), may further experience the trapping-and-detrapping process in the NR[15], leading to a longer τ_2 lifetime. It is possible that the breaking of structural symmetry in the 1D $CsPbBr_3$ NRs will allow additional radiative transitions from symmetry-forbidden states to elongate the observed average PL lifetime[34], which is worthy of further investigation.

Importantly, the PLQYs of all the PS-ligated $CsPbBr_3$ NRs (Fig. 5c,f) are much higher than those of conventional $CsPbBr_3$ NRs of similar sizes prepared through co-capping with octylamine (OctAm) and oleylamine (OAm) (denoted as OctAm–OAm co-capped $CsPbBr_3$ NRs (<1%, in the literature))[15]. The high PLQYs of the PS-ligated $CsPbBr_3$ NRs signify how important it is to eliminate ligand dissociation during

https://doi.org/10.1038/s44160-023-00307-5

the purification and storage of the as-prepared perovskite NRs produced by our nanoreactor platform. Furthermore, it is important to note that the average PL lifetimes of PS-ligated $CsPbBr_3$ NRs are much shorter than those of PS-ligated $CsPbBr_3$ nanoparticles and exhibit a different trend[20], which may be due to the distinctive numbers of PAA chains embedded inside and thus defect densities of the as-prepared $CsPbBr_3$ NCs, as supported by much lowered PLQY of NRs over that of nanoparticles. The effect of PAA chains on the optical properties of $CsPbBr_3$ NCs is worthy of further study.

The 1D structure of perovskite NRs enables polarized optical properties due to uneven electric field strength[16] and different confinement extents of the charge carriers along the radial and axial directions[8]. The linearly polarized light emission of 1D perovskite NRs makes them potentially suitable for use as a backlight in liquid crystal displays[9,16]. The anisotropic factor (R) of the PL of PS-ligated $CsPbBr_3$ NRs was examined using the excitation photoselection PL method[9] and correlated with their tailorable AR values (Supplementary Fig. 23). Specifically, R was determined via $R = (I_{\parallel} - I_{\perp})/(I_{\parallel} + 2I_{\perp}) = (I_{VV} - GI_{VH})/(I_{VV} + 2GI_{VH})$, where $I_{\parallel}$ and $I_{\perp}$ denote the intensity of the polarized PL parallel and perpendicular to the direction of excitation, respectively. The subscripts V (vertical) and H (horizontal) denote the configuration of the polarizer at the excitation (first letter in the subscript) and emission (second letter in the subscript) channels (Supplementary Fig. 23a). The instrument correction factor $G = I_{HV}/I_{HH}$ is used to correct the differential monochromator intensity throughput.

As depicted in Supplementary Fig. 23b,d, the PL intensity of the PS-ligated $CsPbBr_3$ NRs with $D \approx 10.0$ nm and $L = 52.2$ nm (AR ≈ 5) from cellulose-*g*-(PAA-*b*-PS)-2 showed a limited difference between $I_{\parallel}$ and $I_{\perp}$, a low R value of 0.11. Increasing the AR of the $CsPbBr_3$ NRs to ~21 ($D = 10.4$ nm and $L = 217.2$ from cellulose-*g*-(PAA-*b*-PS)-9, via elongating L at a fixed D) yielded a clear drop in $I_{\perp}$ (Supplementary Fig. 23c) and a high R of 0.30 (Supplementary Fig. 23d), owing to the enhanced structural anisotropy of long $CsPbBr_3$ NRs. Reducing the diameter of the $CsPbBr_3$ NRs from 16.2 nm to 12.3 nm, 9.7 nm and 6.6 nm at a fixed length ($L \approx 80$ nm)—that is, increasing the AR—elevated R (Supplementary Fig. 23e). Clearly, enhancing the structural anisotropy by increasing the AR of the $CsPbBr_3$ NRs, through either reducing D or increasing L, leads to improved optical anisotropy. The R value of the PL increased proportionally with the AR of the $CsPbBr_3$ NRs until AR ≈ 10 by varying either the length or the diameter of the NRs, suggesting that the dielectric effect originating from the structural anisotropy of the NRs primarily contributes to the origin of this linearly polarized emission[39]. A further increase in R for the $CsPbBr_3$ NRs may be achieved by introducing lattice distortion[9], manipulating the electronic band structure and exciton recombination[40] or by spatially aligning the NRs into assembly[8].

Stability of PS-ligated perovskite NRs

Owing to the intimate and firm tethering of the PS chains on the surface of individual perovskite NRs, the PS-ligated perovskite NRs created via the platform of cylindrical unimolecular BBCP nanoreactors also afford a set of markedly enhanced stabilities under different conditions, positioning them well for practical applications. For comparison, OctAm–OAm co-capped $CsPbBr_3$ NRs of similar dimensions ($D \approx 10$ nm and $L \approx 90$ nm) synthesized via a conventional hot-injection method[15] were used as a control (Fig. 6 and Supplementary Figs. 24–26).

First, the colloidal stability of the NRs was evaluated. Figure 6a shows the PL peak position of the PS-ligated $CsPbBr_3$ NRs in toluene solution, which remains constant at 513 nm when stored under ambient conditions for 50 days, whereas a drastic change between 503 nm and 528 nm is seen for conventional OctAm–OAm co-capped $CsPbBr_3$ NRs stored under the same conditions. Moreover, the PL intensity of the co-capped $CsPbBr_3$ NRs showed a significant drop during storage and was completely quenched after 50 days (Fig. 6b). This is due to the rapid desorption of OctAm and OAm ligands from the NR surface[19,24],

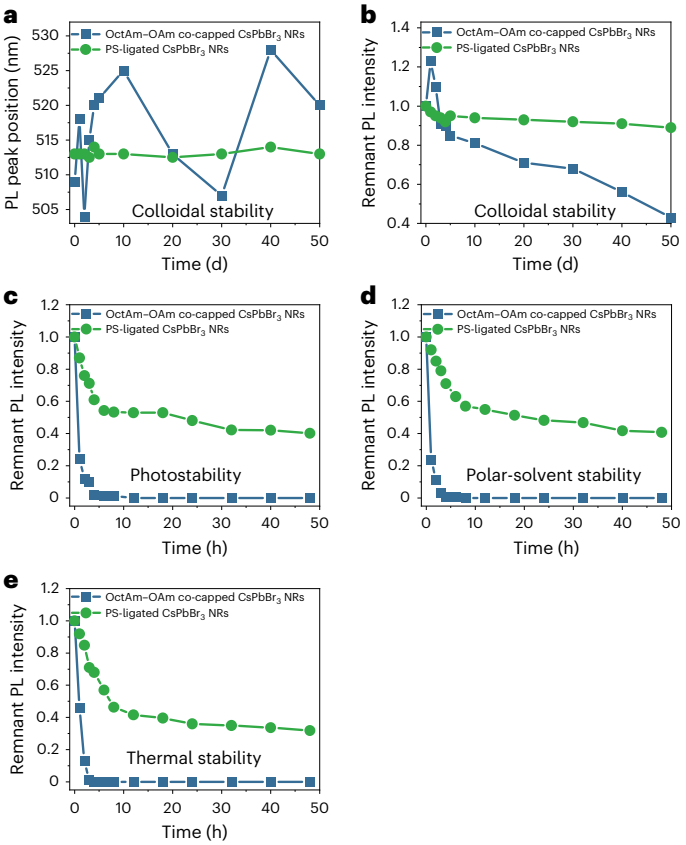

Fig. 6 | Comparison of the stability of PS-ligated $CsPbBr_3$ NRs and OctAm–OAm co-capped $CsPbBr_3$ NRs by monitoring the evolution of the respective PL peak position and PL peak intensity. a,**b**, Colloidal stability of PS-ligated $CsPbBr_3$ NRs and OctAm–OAm co-capped $CsPbBr_3$ NRs in terms of their PL peak position (**a**) and intensity (**b**) in a non-polar solvent (toluene) during storage under ambient conditions. **c**–**e**, Photostability upon UV irradiation (**c**), stability in a polar solvent (**d**) and thermal stability (**e**) of PS-ligated $CsPbBr_3$ NRs and OctAm–OAm co-capped $CsPbBr_3$ NRs in terms of their PL peak intensity.

meaning that the exposed surface is susceptible to moisture under ambient conditions, thereby triggering the generation of defects, severe aggregation and the phase transformation from luminescent $CsPbBr_3$ to non-luminescent $PbBr_2$ and Cs_4PbBr_6 (X-ray diffraction patterns in Supplementary Fig. 26a) during storage[41]. Consequently, the OctAm–OAm co-capped $CsPbBr_3$ NRs were structurally disintegrated, transforming progressively into irregular NCs with a broadened size distribution and agglomeration after, respectively, 30 days (Supplementary Fig. 24b) and 50 days (Supplementary Fig. 24c) of storage. Thus, the emergence of surface defects together with the decomposition and aggregation of co-capped $CsPbBr_3$ NRs led to the vastly changed PL peak position and rapid decay of the PL intensity[20]. By contrast, as a layer of PS chains is intimately and permanently anchored on the NR surface at the single-NR level (Figs. 1 and 4a), the PS-ligated $CsPbBr_3$ NRs retained their uniform 1D morphology (Supplementary Fig. 25) and orthorhombic phase of $CsPbBr_3$ (Supplementary Fig. 26b) after storage under ambient conditions for 50 days. As such, they exhibited a high retention of their PL intensity (>90%) and a constant PL peak position for at least 50 days.

The photostability of the $CsPbBr_3$ NRs against UV irradiation (at a wavelength of 365 nm) was then examined (Fig. 6c). Under continuous UV exposure, the PL intensity of the conventional OctAm–OAm co-capped $CsPbBr_3$ NRs diminished rapidly and disappeared completely in 8 h due to the UV-induced decomposition of $CsPbBr_3$ (ref. 14). Conversely, the PS-ligated $CsPbBr_3$ NRs retained nearly 42%

of their original PL intensity even after UV illumination for 48 h, corroborating the superior photostability of the PS-ligated $CsPbBr_3$ NRs.

The ionic crystal nature of $CsPbBr_3$ makes it prone to decomposition when exposed to solvents of high polarity (such as water and alcohols)[20]. The polar-solvent stability of the $CsPbBr_3$ NRs was inspected by injecting isopropanol into a toluene solution of the NRs (at a volume ratio of isopropanol to toluene of 1:9) with vigorous stirring (Fig. 6d). Upon injection of isopropanol, the OctAm–OAm co-capped $CsPbBr_3$ NRs exhibited a rapid and substantial drop of their PL intensity until complete loss in 3 h. By marked contrast, because of the unfavourable interaction between the hydrophobic PS chains and hydrophilic isopropanol, the outer PS chains collapsed on the surface of the $CsPbBr_3$ NRs, thereby creating a densely packed protective polymeric shell to effectively prevent isopropanol from directly contacting the $CsPbBr_3$ (ref. 20). Even under intense stirring, the PS-ligated $CsPbBr_3$ NRs demonstrated a 38% retention of their original PL intensity.

Subsequently, the thermal stability of the $CsPbBr_3$ NRs was assessed by heating their toluene solution to 50 °C and maintaining it at this temperature for a certain period of time (Fig. 6e). Owing to the pronounced trapping of photogenerated excitons at elevated temperature[42], both the PS-ligated and conventional co-capped $CsPbBr_3$ NRs showed a drop in PL intensity when heated at 50 °C. Clearly, the OctAm–OAm co-capped $CsPbBr_3$ NRs displayed a severe PL loss with complete PL quenching in 5 h, whereas the PS-ligated $CsPbBr_3$ NRs demonstrated a PL retention of >40% at 48 h, which was due possibly to the more considerable dissociation of the OctAm and OAm ligands at elevated temperature[24]. By contrast, owing to the firm ligation of the PS chains on the NRs, as noted above, the PL loss was substantially retarded.

On the basis of this collection of greatly boosted stabilities of the PS-ligated $CsPbBr_3$ NRs over their conventional OctAm–OAm co-capped $CsPbBr_3$ counterpart, such hydrophobic-polymer-ligated perovskite NRs offer appealing opportunities for practical applications in optoelectronics. Further improvement in the stabilities can be readily imparted by growing longer PS chains, increasing the grafting density of the PS chains (via changing BiBB to 3-bromo-2-(bromomethyl) propionic acid to double the grafting density) or coating the $CsPbBr_3$ NR core with a metal oxide shell layer (for example, a SiO_2 shell by exploiting amphiphilic bottlebrush-like triblock copolymers)[43]. In the latter context, such amphiphilic bottlebrush-like triblock copolymers, which are composed of hydrophilic inner and intermediate blocks and hydrophobic outer PS blocks, could direct the respective precursors into the perovskite core and the metal oxide shell (forming a core/shell NR) that is ligated by the outer PS blocks, thereby creating dual-shelled perovskite NRs (that is, protected by the organic PS shell and the inorganic metal oxide shell). This will be the subject of future studies.

Conclusion

In summary, through the leveraging of cylindrical BBCPs as nanoreactors we demonstrated a general platform to create myriad perovskite NRs with fine control over their dimensions and compositions, providing outstanding stabilities under different conditions. An array of perovskite NRs with various diameters ($D \approx 7$–16 nm at a fixed length) and lengths ($L \approx 40$–220 nm at a constant diameter) was produced. All-inorganic perovskite, organic–inorganic perovskite and double-perovskite NRs of the same dimensions can be conveniently prepared. Such morphologically stable, polymer-ligated perovskite NRs show a set of intriguing structure–property relationships. Taking the as-synthesized PS-ligated $CsPbBr_3$ NRs as an example, reducing the NR size radially below its Bohr diameter invokes strengthened quantum confinement and thus a shortened PL lifetime and enhanced PLQY. By sharp contrast, lengthening the $CsPbBr_3$ NR size axially renders the prolonged PL lifetime and decreased PLQY due to the formation of free charge carriers and their subsequent trapping-and-detrapping process. Moreover, the structural anisotropy of the $CsPbBr_3$ NRs is found to correlate well with their optical anisotropy. Owing to the intimate and strong tethering of hydrophobic PS chains on the surface, the PS-ligated perovskite NRs exhibit long-term structural and optical-property stabilities against UV irradiation, polar solvents and elevated temperatures.

Conceptually, the amphiphilic BBCP nanoreactor platform is amenable for the synthesis of virtually unlimited highly stable, polymer-ligated perovskite NRs with precisely controlled dimensions, complex architectures and rich surface chemistry (for example, replacing PS with π-conjugated or stimuli-responsive polymers could enable additional functionality of the outer polymer chains). Such an expanded library of polymer-ligated perovskite NRs may open up exciting possibilities for fundamental research on the optical, photocatalytic and sensory properties that are contingent on their dimensions and compositions, thereby underpinning future advances in light-emitting technologies (such as displays, solid-state lighting and lasers), catalysis and electronics, among other areas.

Methods

Additional details regarding the materials and methods may be found in the Experimental section in the Supplementary Information.

Synthesis of PS-ligated $CsPbBr_3$ NRs using cellulose-*g*-(PAA-*b*-PS) BBCPs as nanoreactors

Briefly, cellulose-*g*-(PAA-*b*-PS) BBCPs (10 mg) were first dissolved in anhydrous DMF (10 ml) under stirring at room temperature for 24 h to yield uniform, stable unimolecular cylindrical micelles, followed by the addition of a suitable amount of CsBr (molar ratio of CsBr:acrylic groups in cellulose-*g*-(PAA-*b*-PS) BBCPs = 1.2:1). It is worth noting that CsBr has a relatively poor solubility in DMF and thus requires additional stirring (for 12 h) to reach complete dissolution. Subsequently, $PbBr_2$ (molar ratio of CsBr:$PbBr_2$ = 1:1) was added to the transparent solution containing the cellulose-*g*-(PAA-*b*-PS) BBCPs and CsBr, with stirring for an additional 24 h. Afterwards, DMF solution (0.5 ml) that contains both the cellulose-*g*-(PAA-*b*-PS) BBCPs and $CsPbBr_3$ precursors (that is, a precursor-loaded cellulose-*g*-(PAA-*b*-PS) BBCP DMF solution) was injected quickly into anhydrous toluene (5 ml) preheated at 50 °C, bringing about the rapid formation of uniform PS-ligated $CsPbBr_3$ NRs. Subsequently, the toluene solution was cooled to room temperature. The PS-ligated $CsPbBr_3$ NRs were isolated by adding ethyl acetate as the poor solvent, with centrifugation at 4,427 × *g* for 5 min. Then, the precipitants were re-dispersed in toluene and centrifuged at 1,107 × g for 5 min to remove the excess precursors and $CsPbBr_3$ forming outside the cellulose-*g*-(PAA-*b*-PS) nanoreactors. This purification process using ethyl acetate as the poor solvent and toluene as the good solvent was conducted as least three times. Since PS imparts good dispersion in toluene, the PS-ligated $CsPbBr_3$ NRs formed a stable colloidal solution in toluene without precipitation.

Data availability

The data reported in this paper are available in the main text or the Supplementary Information. Source data are provided with this paper.

References

1. Swarnkar, A. et al. Quantum dot-induced phase stabilization of α-$CsPbI_3$ perovskite for high-efficiency photovoltaics. *Science* **354**, 92–95 (2016).
2. Dong, Y. et al. Bipolar-shell resurfacing for blue LEDs based on strongly confined perovskite quantum dots. *Nat. Nanotechnol.* **15**, 668–674 (2020).
3. Ma, X. et al. A flexible plasmonic-membrane-enhanced broadband tin-based perovskite photodetector. *Nano Lett.* **21**, 9195–9202 (2021).
4. Shang, Q. et al. Role of the exciton–polariton in a continuous-wave optically pumped $CsPbBr_3$ perovskite laser. *Nano Lett.* **20**, 6636–6643 (2020).

5. Chen, Q. et al. All-inorganic perovskite nanocrystal scintillators. *Nature* **561**, 88–93 (2018).
6. Raja, S. N. et al. Encapsulation of perovskite nanocrystals into macroscale polymer matrices: enhanced stability and polarization. *ACS Appl. Mater. Interfaces* **8**, 35523–35533 (2016).
7. Li, Q., Yang, Y., Que, W. & Lian, T. Size- and morphology-dependent Auger recombination in $CsPbBr_3$ perovskite two-dimensional nanoplatelets and one-dimensional nanorods. *Nano Lett.* **19**, 5620–5627 (2019).
8. Zhang, C. et al. Metal halide perovskite nanorods: shape matters. *Adv. Mater.* **32**, 2002736 (2020).
9. Dou, Y. et al. Lattice distortion in mixed-anion lead halide perovskite nanorods leads to their high fluorescence anisotropy. *ACS Mater. Lett.* **2**, 814–820 (2020).
10. Wang, S. et al. Stable, strongly emitting cesium lead bromide perovskite nanorods with high optical gain enabled by an intermediate monomer reservoir synthetic strategy. *Nano Lett.* **19**, 6315–6322 (2019).
11. Bera, S., Shyamal, S. & Pradhan, N. Chemically spiraling $CsPbBr_3$ perovskite nanorods. *J. Am. Chem. Soc.* **143**, 14895–14906 (2021).
12. He, Y. et al. Dual-protected metal halide perovskite nanosheets with an enhanced set of stabilities. *Angew. Chem. Int. Ed.* **60**, 7259–7266 (2021).
13. Huang, H. et al. Growth mechanism of strongly emitting $CH_3NH_3PbBr_3$ perovskite nanocrystals with a tunable bandgap. *Nat. Commun.* **8**, 996 (2017).
14. Shamsi, J., Urban, A. S., Imran, M., De Trizio, L. & Manna, L. Metal halide perovskite nanocrystals: synthesis, post-synthesis modifications, and their optical properties. *Chem. Rev.* **119**, 3296–3348 (2019).
15. Gao, M. et al. Scaling laws of exciton recombination kinetics in low dimensional halide perovskite nanostructures. *J. Am. Chem. Soc.* **142**, 8871–8879 (2020).
16. Li, Y. et al. Using polar alcohols for the direct synthesis of cesium lead halide perovskite nanorods with anisotropic emission. *ACS Nano* **13**, 8237–8245 (2019).
17. Yang, D. et al. Interfacial synthesis of monodisperse $CsPbBr_3$ nanorods with tunable aspect ratio and clean surface for efficient light-emitting diode applications. *Chem. Mater.* **31**, 1575–1583 (2019).
18. Wang, Y. et al. Reversible transformation between $CsPbBr_3$ perovskite nanowires and nanorods with polarized optoelectronic properties. *Adv. Funct. Mater.* **31**, 2011251 (2021).
19. Akkerman, Q. A., Rainò, G., Kovalenko, M. V. & Manna, L. Genesis, challenges and opportunities for colloidal lead halide perovskite nanocrystals. *Nat. Mater.* **17**, 394–405 (2018).
20. Yoon, Y. J. et al. Enabling tailorable optical properties and markedly enhanced stability of perovskite quantum dots by permanently ligating with polymer hairs. *Adv. Mater.* **31**, 1901602 (2019).
21. Roy, D., Semsarilar, M., Guthrie, J. T. & Perrier, S. Cellulose modification by polymer grafting: a review. *Chem. Soc. Rev.* **38**, 2046–2064 (2009).
22. Pang, X., He, Y., Jung, J. & Lin, Z. 1D nanocrystals with precisely controlled dimensions, compositions, and architectures. *Science* **353**, 1268–1272 (2016).
23. Pang, X., Zhao, L., Han, W., Xin, X. & Lin, Z. A general and robust strategy for the synthesis of nearly monodisperse colloidal nanocrystals. *Nat. Nanotechnol.* **8**, 426–431 (2013).
24. De Roo, J. et al. Highly dynamic ligand binding and light absorption coefficient of cesium lead bromide perovskite nanocrystals. *ACS Nano* **10**, 2071–2081 (2016).
25. Zhang, D., Eaton, S. W., Yu, Y., Dou, L. & Yang, P. Solution-phase synthesis of cesium lead halide perovskite nanowires. *J. Am. Chem. Soc.* **137**, 9230–9233 (2015).
26. Li, W. et al. Chemically diverse and multifunctional hybrid organic–inorganic perovskites. *Nat. Rev. Mater.* **2**, 16099 (2017).
27. Fan, Q. et al. Lead-free halide perovskite nanocrystals: crystal structures, synthesis, stabilities, and optical properties. *Angew. Chem. Int. Ed.* **59**, 1030–1046 (2020).
28. Shi, Y. et al. Noble-metal nanocrystals with controlled shapes for catalytic and electrocatalytic applications. *Chem. Rev.* **121**, 649–735 (2020).
29. Liu, W. et al. Mn^{2+}-doped lead halide perovskite nanocrystals with dual-color emission controlled by halide content. *J. Am. Chem. Soc.* **138**, 14954–14961 (2016).
30. Zhu, H. et al. One-dimensional highly-confined $CsPbBr_3$ nanorods with enhanced stability: synthesis and spectroscopy. *Nano Lett.* **22**, 8355–8362 (2022).
31. Lan, Y.-F. et al. Spectrally stable and efficient pure red $CsPbI_3$ quantum dot light-emitting diodes enabled by sequential ligand post-treatment strategy. *Nano Lett.* **21**, 8756–8763 (2021).
32. Pradhan, N. Do halide perovskites prefer a specific direction for forming one-dimensional nanostructures? *ACS Energy Lett.* **7**, 150–153 (2021).
33. Protesescu, L. et al. Nanocrystals of cesium lead halide perovskites ($CsPbX_3$, X=Cl, Br, and I): novel optoelectronic materials showing bright emission with wide color gamut. *Nano Lett.* **15**, 3692–3696 (2015).
34. Krieg, F. et al. Monodisperse long-chain sulfobetaine-capped $CsPbBr_3$ nanocrystals and their superfluorescent assemblies. *ACS Cent. Sci.* **7**, 135–144 (2020).
35. Shinde, A., Gahlaut, R. & Mahamuni, S. Low-temperature photoluminescence studies of $CsPbBr_3$ quantum dots. *J. Phys. Chem. C* **121**, 14872–14878 (2017).
36. Hintermayr, V. A. et al. Tuning the optical properties of perovskite nanoplatelets through composition and thickness by ligand-assisted exfoliation. *Adv. Mater.* **28**, 9478–9485 (2016).
37. Bohn, B. J. et al. Boosting tunable blue luminescence of halide perovskite nanoplatelets through postsynthetic surface trap repair. *Nano Lett.* **18**, 5231–5238 (2018).
38. Rabouw, F. T. et al. Delayed exciton emission and its relation to blinking in CdSe quantum dots. *Nano Lett.* **15**, 7718–7725 (2015).
39. Shabaev, A. & Efros, A. L. 1D exciton spectroscopy of semiconductor nanorods. *Nano Lett.* **4**, 1821–1825 (2004).
40. Planelles, J., Rajadell, F. & Climente, J. I. Electronic origin of linearly polarized emission in CdSe/CdS dot-in-rod heterostructures. *J. Phys. Chem. C* **120**, 27724–27730 (2016).
41. Liu, Z. et al. Ligand mediated transformation of cesium lead bromide perovskite nanocrystals to lead depleted Cs_4PbBr_6 nanocrystals. *J. Am. Chem. Soc.* **139**, 5309–5312 (2017).
42. Diroll, B. T., Zhou, H. & Schaller, R. D. Low-temperature absorption, photoluminescence, and lifetime of $CsPbX_3$ (X=Cl, Br, I) nanocrystals. *Adv. Funct. Mater.* **28**, 1800945 (2018).
43. He, Y. et al. Unconventional route to dual-shelled organolead halide perovskite nanocrystals with controlled dimensions, surface chemistry, and stabilities. *Sci. Adv.* **5**, eaax4424 (2019).

Acknowledgements

This work is supported by the following funding: Air Force Office of Scientific Research grant FA9550-19-1-0317 (Z.L.), National Science Foundation grant DMR 1903990 and CHE 1903957 (Z.L.) and National Science Foundation grant CHE 2004080 (T.L.).

Author contributions

Z.L. conceived the idea and supervised the work. S.L., M.Z., S.H., M.T. and W.C. carried out the experiments. S.L., M.Z., S.H., M.T., W.C., T.L. and Z.L. analysed and discussed the data and results. Z.L. and S.L. wrote the original draft.

Competing interests
The authors declare no competing interests.

Additional information
Supplementary information The online version contains supplementary material available at https://doi.org/10.1038/s44160-023-00307-5.

Correspondence and requests for materials should be addressed to Zhiqun Lin.

Peer review information *Nature Synthesis* thanks Qiao Zhang and the other, anonymous, reviewer(s) for their contribution to the peer review of this work. Primary handling editor: Alexandra Groves, in collaboration with the *Nature Synthesis* team.